Engineering Structures 273 (2022) 115106

Contents lists available at ScienceDirect

Engineering Structures

journal homepage: www.elsevier.com/locate/engstruct

Analytical model for evaluating lateral force capacity of precast concrete-filled steel tube column

Kaidi Zhang [a], Junfeng Jia [a,*], Ning Li [b], Jianyu Zhao [c], Yulei Bai [a]

[a] Key Laboratory of Urban Security and Disaster Engineering of Ministry of Education, Beijing University of Technology, Beijing 100124, China
[b] Key Laboratory of Earthquake Engineering Simulation and Seismic Resilience of China Earthquake Administration (Tianjin University), Tianjin 300350, China
[c] China ENFI Engineering Corporation, Beijing 100038, China

ARTICLE INFO

Keywords:
Precast segmental bridge column
Simplified model
Lateral force–displacement relationship
Neutral axis depth
Finite element analysis
Nonlinear regression

ABSTRACT

Precast segmental columns have been frequently applied in regions of low seismicity due to rapid construction, high quality, and low downtime. Their lateral force–displacement curves were always calculated using iterative models in former studies, which could be time-consuming and arduous. Whereas, a non-iterative model can greatly improve computational efficiency and is preferred by designers. In this study, a non-iterative simplified analytical model was firstly proposed considering different neutral axis depths of the rocking interface. The neutral axis depth approached a constant value during lateral loading according to the results of the former tests and numerical studies. Then, a quasi-static test and finite element model of a precast segmental concrete-filled steel tube (PS-CFST) column were conducted to verify the proposed analytical model. Based on the finite element model, a nonlinear regression equation was set up to predict the constant neutral axis depth of the PS-CFST column according to the simulation results of 48 cases. Finally, the influence of the initial prestressing force, area of the prestressed tendons and gravity load on the lateral force capacity of the PS-CFST column were investigated. It was concluded that the constant value of neutral axis depth was positively related to axial ratio and diameter-thickness ratio, and negatively related to yield strength of steel tube of PS-CFST columns. The analytical model without iteration proposed in this study was appropriate to predict lateral force capacity of post-tensioned precast segmental columns, and it had a favorable agreement with testing and numerical results. Furthermore, the precast column with the lower gravity load and the higher reinforcement ratio of prestressed tendons would result in the larger post-yield stiffness.

1. Introduction

With the merits of rapid construction, high quality, high engineering safety and low environmental impact, precast segmental columns have been mostly applied in regions of low and medium seismicity[1–2], such as Linn Cove Viaduct, Hoover Dam Bypass Bridge, Sunshine Skyway Bridge, Victory Bridge and Wigram Magdala Link Bridge in New Zealand, etc. Huangxulu Overpass Bridge was recently built in Beijing, with the first columns connected by unbonded post-tensioning (PT) tendons in China[3].

The seismic performance of post-tensioned precast columns subjected to quasi-static cyclic loading was fully studied. Mander and Cheng [4] firstly investigated the seismic performance of precast segmental bridge columns. Serious damage was found in the plastic hinge zone of the columns, leading to a decrease in lateral strength. To minimize the damage to the plastic hinge zone and local stress concentration after the earthquake, high transverse reinforcement ratio[4], steel tubes[5–8], and high-performance materials including fiber reinforced plastic (FRP) [9], ultra-high performance concrete (UHPC)[10] and fiber reinforced concrete (FRC)[11] were adopted to fabricate the bottom or all segments of the precast segmental bridge columns. In addition to serious damage to the bottom segment, poor energy dissipation (ED) capacity was also the reason why precast segmental columns were limited in low seismic zones[12]. To increase the ED capacity of precast columns, continuous bonded mild steel rebars[112–14], shape memory alloys (SMA)[16–18], and high-strength bars[19] across the segments were developed. Besides, various replaceable external ED devices were proposed as an alternative option for ED bars[31021–25], e.g. aluminum bars, steel angle dampers, buckling-restrained plates and UHPC panels.

The research on the seismic performance of precast segmental columns aforementioned was generally conducted by quasi-static cycling

* Corresponding author.
E-mail address: jiajunfeng@bjut.edu.cn (J. Jia).

https://doi.org/10.1016/j.engstruct.2022.115106
Received 11 March 2022; Received in revised form 17 September 2022; Accepted 7 October 2022
Available online 21 October 2022

Nomenclature

A List of symbols

D	Width of column cross-section
C_4	Neutral axis depth at the constant depth stage
F_{si}	Initial prestressing force
P	Gravity load
A	Cross-sectional area of the column
h	Height of the column
I_g	Moment of inertia of the column
F_1	Lateral force at the end of the full depth stage
Δ_1	Displacement at the end of the full depth stage
ϕ_1	Curvature at the end of the full depth stage
E	Elastic modulus
E_c	Elastic modulus for concrte
E_{sc}	Elastic modulus for concrete-filled steel tube
A_s	Cross-sectional area of steel pipe
A_c	Cross-sectional area of concrete
F_2	Lateral force at the end of the linear reduced depth stage
$I_{g/2}$	Moment of inertia of the column at the end of the linear reduced depth stage
Δ_2	Displacement at the end of the linear reduced depth stage
Δ_{2e}	Elastic displacement at the end of the linear reduced depth stage
Δ_{2p}	Plastic displacement at the end of the linear reduced depth stage
L_p	Length of the plastic hinge
ϕ_2	Curvature at the end of the linear reduced depth stage
d	Distance from the centroid of the compression zone to the edge of the section
F_4	Lateral force at the constant depth stage
Δ_4	Displacement at the constant depth stage
N	Total axial compression ratio
F_s	Total prestressing force
ΔF_{si}	Increment of prestressing force
θ	Rotation angle of the column
Δ_b	Lateral displacement of the edge of the column top at the constant depth stage
Δl	Elongation of prestressed tendons
Δ_4	Lateral displacement of the center of the column top
E_p	Elastic modulus of prestressed tendons
A_p	Across-section area of prestressed tendons
l	Length of prestressed tendons
k_p	Equivalent axial stiffness of the prestressed tendons
Δ_R	Displacement caused by rigid body rotation
Δ_θ	Displacement caused by bending deformations
Δ_v	Displacement caused by shear deformations
η	Reduction coefficient of the elongation of prestressed tendons
K_θ	Flexural stiffness of the column
K_V	Shear stiffness of the column
μ_c	Concrete poisson ratio
μ_s	Steel poisson ratio
β	Reduction coefficient of neutral axis depth on the elongation of prestressed tendons
$\Delta l'$	Real elongation of prestressed tendons
λ	Reduction coefficient of the axial deformation of the column
Δh	Elongation of the column

loading. The dynamic response was also increasingly investigated by researchers with pseudo-dynamic[26] and shake table tests[27–30], even including underwater shake table tests[31]. These studies proved that the precast segmental bridge column was slightly damaged under earthquake motions. Meanwhile, the seismic performance of post-tensioned precast bridges was compared with cast-in-place bridges, the result indicated that the cast-in-place bridges suffered major concrete spalling and fracture of longitudinal and transverse rebars, whereas damage to concrete was only cosmetic and facture was limited to longitudinal rebars for post-tensioned precast bridges[28]. In further investigating the seismic performance of precast segmental columns, a few scholars[1432–35] have studied the response of columns subjected to bidirectional loading through the quasi-static test, shake table test, and numerical evaluation methods. Sometimes, to improve the loading efficiency, several researchers adopted unidirectional oblique lateral loading instead of complicated biaxial loading. They found that the direction of seismic loads had a significant effect on the overall structural performance[1432]. The study of Reza[32] et al indicated that the precast columns loaded along the strong axis had a larger capacity, but a worse ductile response and more serious concrete damage compared with those loaded along the weak axis. Jia et al[14] suggested that nonorthogonal oblique loading should be considered in the design of precast columns, because a larger residual displacement was found when subjected to nonorthogonal oblique loading. Li et al[33] obtained a similar conclusion through numerical simulation. To compare the dynamic response of cast-in-place monolithic and precast segmental columns under bidirectional earthquake motions, Li et al[34] carried out shake table tests. The results indicated that more serious damage was observed in the cast-in-place monolithic column, whereas non-negligible twisting was found in the precast column. The reason was that the friction force between the joints was not enough for countering the torsional moment under the bidirectional earthquake motions. Therefore, the torsion of joints between segments is noteworthy for the precast segmental columns.

Fiber-section numerical models and finite element models were frequently used to evaluate the seismic performance of precast segment columns under lateral loading. Fiber-section models could accurately simulate the nonlinear response of precast columns under quasi-static and dynamic loading, but could not precisely simulate the deformation behavior of the column and the stress distribution of joints. This problem could be overcome by finite element models. With the improvement of computer calculation efficiency, the main design parameter analysis of precast segmental columns was frequently investigated by numerical simulation, and sometimes by experiments. The main design parameters comprised the area ratio of ED rebars, the initial prestressing level of PT tendons, the vertical gravity loading, the bonding conditions of PT tendons, and the position configuration of PT tendons. Many scholars[1,13,15,36–38] studied the effect of the area ratio of ED rebars on the seismic performance of precast segmental columns and concluded that the ED capacity and residual displacement increased with the area ratio. To maintain self-centering capacity, λ_{ED}, which was the factor of the ED reabar contribution to the expected column strength, was defined by Ou et al[1], and less than 35 % was recommended. A high initial prestressing level of PT tendons resulted in high strength and self-centering capacity, but excessive initial prestress level may lead to a large loss of prestressing and yield prematurely [15243639–40]. Thence, the initial prestressing level of PT should be less than 60 % of yield strength as recommended by Zhang et al[39]. A high vertical gravity loading also brought a high strength, differently, the post-yield stiffness decreased with increasing vertical gravity loading[3941] Li et al, Wang et al[41] and Bu et al[15] numerically and experimentally investigated the effect of the bonding conditions of prestressing tendons on the seismic behavior, they concluded that the columns with unbonded PT tendons had smaller residual displacement

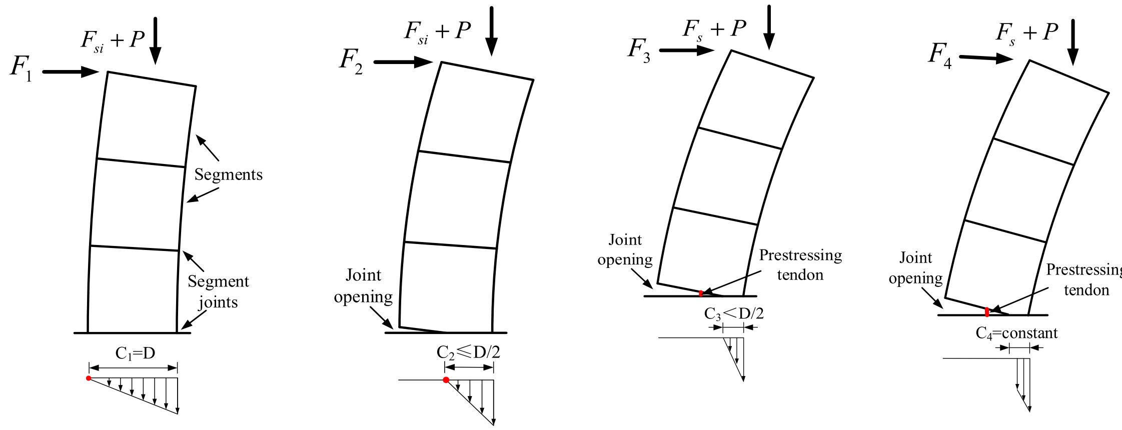

(a) Full depth stage

(b) Linear reduced depth stage

(c) Nonlinear reduced depth stage

(d) Constant depth stage

Fig. 1. Response of precast segmental bridge column at key stages.

and better ductility, but lower lateral strength and ED capacity than those with bonded PT tendons. Zhang et al[43] numerically studied the influence on the hysteretic behavior of PT positions, the lateral capacity and ED capacity for offset configuration of PT tendons increased slightly than the central configuration, whereas the prestressing force increased substantially, which was close to the yield strength when the column was subjected to maximum drift.

An analytical model was firstly proposed by Hewes[5] to describe the lateral force–displacement curves of unbonded post-tensioned precast columns under horizontal loading. Three key stages were defined according to different neutral axis depths. Chou et al.[6] developed a double-plastic hinge model to estimate the seismic behavior of precast columns with unequal height segments. Bu et al.[42–44] established a single-joint model and a multi-joint rotation model of the precast column with ED bars based on the moment–curvature relationship, and the accuracy of the multi-joint rotation model was better than the single-joint rotation model. Ou et al.[13] introduced the concept of decompression region and proposed a simplified analytical method to investigate the mechanical behavior of precast segment columns with energy dissipation devices under lateral loading. The models proposed above can accurately predict the response of precast columns under lateral load. However, these models were iterative because of the uncertainty of the neutral axis depth, increasing the computational cost. A non-iterative model can greatly improve computational efficiency and thus is preferred by designers. Wang et al.[46] proposed a non-iterative analytical model to predict the response of unbonded post-tensioned precast columns with ED bars. Three stages, namely decompression, the yield of ED bars and large deformation were defined in the analytical model. At decompresssion stage, the precast segmental column was considered as the equivalent cast-in-place column. Whereas the neutral axis depth was calculated by complicated force balance equations at the other two stages. Thence, a simplified non-iterative analytical model can be developed to efficiently evaluate the force–displacement response of precast segmental bridge columns, especially for precast segmental concrete-filled steel tube (PS-CFST) columns, which enhance the confinement of concrete, avoid the need for rebar cages and formwork, and have less damage and excellent seismic performance under lateral loading.

In this study, a simplified non-iterative analytical model was firstly derived based on the plane-section assumption, moment–curvature relationship and rotation of a rigid body. Four key stages were defined according to different neutral axis depths. It was found from previous experiments that the neutral axis depth approached a constant value during lateral loading at the last stage. Then, a quasi-static test and finite element model of a PS-CFST column were conducted to verify the proposed analytical model. Based on the validated finite element model, a nonlinear regression equation was set up based on the simulation results of 48 cases to predict the constant neutral axis depth of the PS-CFST at the last stage. Finally, the influences of the area of the prestressed tendons, gravity load and initial prestress on the lateral force capacity of precast segmental bridge columns were investigated.

2. Simplified analytical model for precast segmental columns

The behavior of a precast segment column under lateral loading differs substantially from that of a conventional reinforced concrete (RC) column. In the RC column, the location of concentrated inelastic response is generally in the bridge columns in the form of plastic hinges, where concrete crushing and reinforcement yielding work together to dissipate energy under earthquake loading. In the precast column, large structural deformations are not due to plastic deformation within a plastic hinge zone, but to a rigid rotation of the whole column around its base. The response of a precast column is similar to that of a rocking foundation, which lifts off the ground once the moment resistance provided by a vertical load is overcome. In the study, a simplified non-iterative analytical model, which was divided into four key stages, was deduced for predicting the lateral force capacity of a precast segmental column. The response of a precast column subjected to lateral loading at four stages is shown in Fig. 1. According to the changing trend of the neutral axial depth, the stages are named full depth stage, linear reduced depth stage, nonlinear reduced depth stage and constant depth stage. In the figure, and through this study, the prestressing tendon is located at the mid-depth of the cross-section. As shown in Fig. 1(a), the stress in concrete at the edge of the base joint is zero, which represents the end of the full depth stage. The response of the column is similar to that of the equivalent conventional reinforced concrete column. As lateral displacement increases, the opening of the interface between the foundation and column appears and extends to the section depth. Eventually, the opening reaches the mid-depth of the section, as shown in Fig. 1(b). This condition defines as the end of the linear reduced depth stage, which also represents the beginning of significant nonlinearity. Then, as shown in Fig. 1(c), when the neutral axis depth is less than the mid-depth of the section, the prestressing tendons are stretched and the prestressing force increases. This condition defines the nonlinear reduced depth stage. The prestressing force during the earthquake loading remains elastic if the initial stress is carefully selected. If the

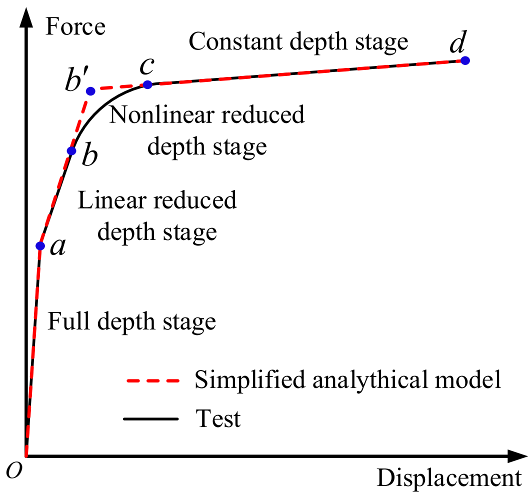

Fig. 2. Force-displacement curve of a precast segmental bridge column.

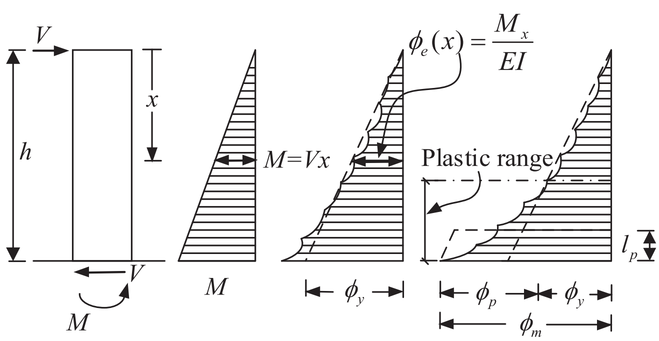

Fig. 3. Simple beam theory.

initial stress is too high, or if the maximum column displacement is larger than expected, the yield of prestressing tendons can occur. It is important to note that the prestressing tendon is the critical component of the precast segment column, its yield greatly affects the seismic performance of the precast segmental bridge column. Thence, the initial stress of the prestressing tendon should be carefully selected. With a further increase in lateral displacement, the neutral axis depth eventually tends to remain virtually unchanged during lateral loading, which is found from references[342]. This condition is defined as the constant depth stage, as shown in Fig. 1(d).

The theoretical lateral force–displacement curve of the precast column is depicted in Fig. 2. The key stages of response described previously are indicated by points *a,b,c,d* in the figure. The response of the full depth and linear reduced depth stages is a linear-elastic relationship, whereas that of the nonlinear reduced depth and constant depth stages is non-linear. Complex iterative analysis is required to obtain the neutral axis depth of the nonlinear reduced depth stage due to elongation of prestressed tendons. To avoid iterative calculations, the lateral force–displacement relationships at the nonlinear reduced depth and constant depth stages are obtained based on the below simplification and hypothesis:

3. The yielding of prestressing tendons does not occur during the loading process.

2. The lateral force–displacement relationship at the nonlinear reduced depth stage is obtained by extending the lines of the linear reduced depth and constant depth stages. As shown in Fig. 3, both lines *bb*’ and *b*’*c* represent the response of the column at the nonlinear reduced depth stage.

3. The neutral axis depth at the constant depth stage is assumed to be constant[342].

4. For precast segmental columns without external ED devices, only the bottom joint opening is considered because other joint openings are neglected[151015].

3.1. Full depth stage

As presented above, at the full depth stage, the plane-section assumption and the moment–curvature analysis are adopted to obtain the lateral force–displacement relationship. The condition of the end of the full depth stage, point *a*, is that the compressive strain of the concrete at the edge of the column bottom section is zero. Eq. (1) can be calculated as.

$$0.5D\frac{F_1 h}{I_g} = \frac{F_{si} + P}{A} \tag{1}$$

where F_{si} is the initial prestressing force; P is the gravity load; A is the cross-sectional area of the column; h is the column height; I_g is the geometrical moment of inertia, for PS-CFST, $I_g = I_c + I_s$, I_c and I_s are the inertia moment of section of concrete and steel tube of the PS-CFST, respectively.

The lateral force F_1 at the top of the column at point a can be expressed as.

$$F_1 = \frac{(F_{si} + P)I_g}{0.5DAh} \tag{2}$$

The displacement Δ_1 of point a is calculated using simple beam theory, as shown in Fig. 3:

$$\Delta_1 = \frac{1}{3}\phi_1 h^2 \tag{3}$$

$$\phi_1 = \frac{F_1 h}{EI_g} \tag{4}$$

Where ϕ_1 is the curvature of the column bottom at point a, E is the elastic modulus. It should be noted that the formula for calculating the elastic modulus of concrete-filled steel tube is different from that of reinforced concrete. For precast reinforced concrete columns, E is generally replaced by the elastic modulus of concrete (E_c). Whereas, for PS-CFST columns, the confinement effect of steel tube on core concrete, which is highly related to steel ratio α_{sc}, can’t be ignored. According to Technical Code Provision for CFST Structures (GB 50936–2014) in China[51], E of concrete-filled steel tube can be predicted as.

$$E = \frac{(1 + \delta/n)(1 + \alpha_{sc})}{(1 + \alpha_{sc}/n)(1 + \delta)} \times 1.3k_E f_{sc} \tag{5}$$

$$\delta = \frac{I_s}{I_c} \tag{6}$$

$$n = \frac{E_c}{E_s} \tag{7}$$

$$\alpha_{sc} = \frac{A_s}{A_c} \tag{8}$$

Where E_s is the elastic modulus of the steel tube. A_s and A_c are the cross-sectional area of the steel tube and concrete. k_E is the conversion factor, f_{sc} is the compression strength of PS-CFST. k_E and f_{sc} can be obtained by Technical Code Provision for CFST Structures (GB 50936–2014)in China[47].

When Eq. (4) is substituted into Eq. (3).

$$\Delta_1 = \frac{F_1 h^3}{3EI_g} \tag{9}$$

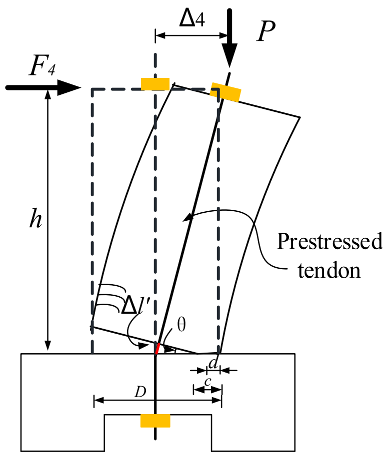

Fig. 4. Behavior of precast column under lateral loading at the constant depth stage.

3.2. Linear reduced depth stage

The force F_2 at the end of the linear reduced depth stage, point b, is given based on the zero stress at the middle of the column bottom interface.

$$\frac{F_2h - y(F_{si} + P)}{I_{g/2}}y = \frac{2(F_{si} + P)}{A} \tag{10}$$

Where y is the distance from the centroid of the compression zone to the middle of the bottom interface; $I_{g/2}$ is the moment of inertia at the end of the linear reduced depth stage. Eq. (10) can be converted to.

$$F_2 = \frac{2(F_{si} + P)I_{g/2}}{Ayh} + \frac{y(F_{si} + P)}{h} \tag{11}$$

The displacement Δ_2 of point b contains the elastic displacement Δ_{2e} and plastic displacement Δ_{2p}. Δ_2 can be calculated as.

$$\Delta_2 = \Delta_{2e} + \Delta_{2p} \tag{12}$$

The elastic displacement Δ_{2e} can be deduced according to the linear lateral force–displacement relationship at the full depth stage (Line oa in Fig. 3).

$$\Delta_{2e} = \frac{F_2}{F_1}\Delta_1 \tag{13}$$

The plastic displacement can be predicted by Eq. (14)[5].

$$\Delta_{2p} = \left[\phi_2 - \frac{F_2}{F_1}\phi_1\right]L_ph \tag{14}$$

where L_p is the length of the plastic hinge; ϕ_2 is the curvature of the bottom section at point b. The values of L_p and ϕ_2 can be obtained by Eq. (15)[13] and Eq. (16)[5], respectively.

$$L_p = \frac{D}{2} \tag{15}$$

$$\phi_2 = \frac{F_2h - y(F_{si} + P)}{EI_{g/2}} \tag{16}$$

Substitute Eqs. (9), (13), (14), (15), (16) into Eq.(12), the displacement Δ_2 at point b can be converted to.

$$\Delta_2 = \frac{2F_2h^3 - 3DF_2h^2}{6EI_g} + \frac{DF_2h^2 - yDh(F_{si} + P)}{2EI_{g/2}} \tag{17}$$

The linear reduced depth stage ends when the neutral axis depth reaches the mid-depth of the section. At the nonlinear reduced depth stage, line bc is simplified to lines bb' and $b'c$, where bb' is the extension of ab, and $b'c$ is the extension of cd. Thus, only the lateral force–displacement relationship of the constant depth stage needs to be calculated for obtaining the response of the column under lateral loading. But the deformation of the column at the constant depth stage is not consistent with the plane-section assumption, and moment–curvature analysis was not adopted to obtain the force–displacement relationship of the constant depth stage. Instead, the analysis is based on the rotation of a rigid body.

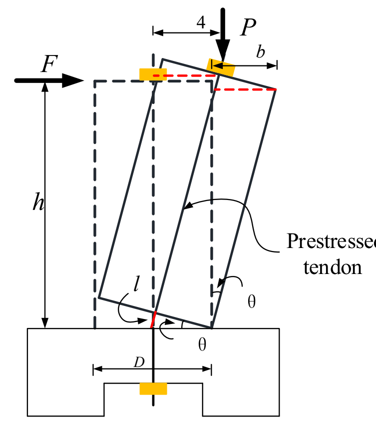

Fig. 5. Rigid body rotation under lateral loading.

3.3. Nonlinear reduced depth and constant depth stages

As shown in Fig. 4, based on the moment equilibrium about the center of the compression zone, Eq. (18) is obtained.

$$P\left(\frac{D}{2} - d - \Delta_4\right) + F_s\left(\frac{D}{2} - d\right) = F_4h \tag{18}$$

The force F_4 at the constant depth stage can be given as.

$$F_4 = \frac{P(D/2 - d - \Delta_4) + F_s(D/2 - d)}{h} \tag{19}$$

$$C_4 = \frac{1.3\sqrt{N}}{\sqrt{7.7}}D \tag{20}$$

Where d is the distance from the centroid of the compression zone to the edge of the column cross-section (as illustrated in Fig. 4), d is respectively equal to $C_4/2$ and $C_4 - 4C_4/3\pi$ for rectangle and circle section, C_4 is the neutral axis depth at the constant depth stage, which is considered a constant. It can be estimated by Eq.(20) for SC-PSBC[42]. For PS-CFST, C_4 will be obtained by a nonlinear regression analysis based on numerical simulation as described below. Where N is the axial compression ratio of the precast column. F_s represents the total prestressing force, which contains the initial prestressing force and the increasing force resulting from the elongation of prestressed tendons, it can be calculated as.

$$F_s = F_{si} + \Delta F_{si} \tag{21}$$

Where ΔF_{si} is the increasing prestressing force, which is calculated as shown below.

Serious damage and opening occurred at the bottom segment, whereas that was minor in other segments for SC-PSBC and PS-CFST [151015]. Thus, the damage and opening between other segments were ignored. At the constant depth stage, the increase of prestressing force is easy to calculate when the whole column is considered a rigid body. As shown in Fig. 5, the geometric relationship between the interface rotation angle θ and the lateral displacement of the edge of the column top Δ_b is shown below.

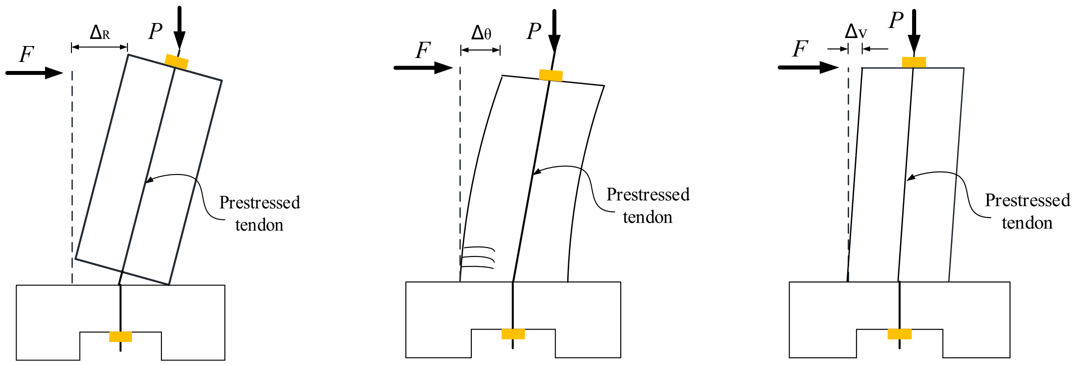

a) Rigid body rotation b) Bending deformation c) Shear deformation

Fig. 6. Deformation of the precast column under lateral loading.

$$\sin\theta = \frac{\Delta_b}{h} \tag{22}$$

The relationship between the lateral displacement of the center (Δ_4) and the edge (Δ_b) of the column top can be expressed by Eq. (23). $\Delta_4 \approx \Delta_b$ since θ is small.

$$\Delta_4 = \Delta_b + 0.5D(1-\cos\theta) \tag{23}$$

The elongation of prestressed tendons Δl is calculated as.

$$\Delta l = 0.5D\sin\theta \tag{24}$$

When the prestressing tendon is elastic, the relationship between the lateral displacement Δ_4 of the column top and the increase of prestressing force ΔF_{si} is expressed as follows:

$$\Delta F_{si} = \frac{0.5D\sin\theta E_p A}{l} = k_p\Delta_4 \tag{25}$$

$$k_p = \frac{0.5DE_pA_p}{hl} \tag{26}$$

In which, E_p is the elastic modulus of prestressed tendons; A_p is the cross-sectional area of prestressed tendons; l is the length of prestressed tendons; k_p is the equivalent axial stiffness of prestressed tendons corresponding to the lateral displacement of the column top.

However, the column is not a rigid body. It will undergo deformation during the rotation of the column around its base: (1) the flexural and shear deformation of the column; (2) the axial deformation of the column caused by prestressed tendons; (3) the deformation of the section at the column bottom.

As shown in Fig. 6, the total lateral displacement of the column Δ_4 comprises the displacement Δ_R due to the rigid body rotation, the displacements $\Delta_{\hat{l}}$ and Δ_v caused by bending and shear deformations of column segments respectively. Therefore, Δ_4 can be given as.

$$\Delta_4 = \Delta_\theta + \Delta_v + \Delta_R = \frac{F_4}{K_\theta} + \frac{F_4}{K_V} + \Delta_R \tag{27}$$

As shown in Fig. 6b and 6c, the bending and shear deformations of the column do not lead to the elongation of prestressed tendons. Therefore, it is necessary to define a coefficient η to revise Δ_4 in Eq. (25):

$$\eta = \frac{\Delta_R}{\Delta_4} \tag{28}$$

Substituting Eq. (27) into Eq. (28) gets:

$$\eta = 1 - \frac{F_4(K_\theta + K_V)}{K_\theta K_V \Delta_4} \tag{29}$$

Where K_θ and K_V are the flexural stiffness and shear stiffness of the column, which can be predicted by Eqs. (30)-(32). Eq. (30) can obtain the flexural stiffness of the SC-PSBC and PS-CFST. Eqs. (31) and (32) can obtain the shear stiffness of the SC-PSBC and PS-CFST, respectively.

$$K_\theta = \frac{2.1EI_g}{h^3} \tag{30}$$

$$K_V = \frac{E_cA}{2(1+\mu_c)h} \tag{31}$$

$$K_V = \frac{E_cA_{cc}}{2(1+\mu_c)h} + \frac{E_sA_{sc}}{2(1+\mu_s)h} \tag{32}$$

A_{cc} and A_{sc} are the areas of the compression zone for the concrete and steel tube of PS-CFST; μ_c and μ_s are the Poisson ratio of the concrete and steel tube, respectively.

When the large joint opening emerges, stress concentration occurs at the compression zone of the column under lateral loading. The column does not rotate about its outermost edge, but rather, rotates around the edge of the compression zone. The real elongation of the prestressed tendons caused by the rotation of the entire column is smaller than that caused by the rotation of the rigid body. To obtain the actual elongation of prestressed tendons, coefficient β is defined to consider the influence of the neutral axis depth on the elongation of the prestressed tendons. β can be calculated as follows:

$$\beta = \frac{\Delta l'}{\Delta l} \tag{33}$$

Where $\Delta l'$ is the actual elongation of prestressed tendons; Δl is the elongation of prestressed tendons when the column rotates about the outermost edge. $\Delta l'$ and Δl can be calculated based on the geometrical relationship (Fig. 5 and Fig. 6).

$$\Delta l = 0.5D\sin\theta \tag{34}$$

$$\Delta l' = (0.5D - C_4)\sin\theta \tag{35}$$

Substituting Eqs. (34), (35) into Eq. (33) gives.

$$\beta = 1 - \frac{2C_4}{D} \tag{36}$$

β is related to the neutral axis depth. β is equal to 1 if the neutral axis depth C_4 is infinitesimally small, the structure is similar to a rigid body. β decreases with the increase of C_4.

The axial deformation of the column and prestressed tendons will affect each other. The increasing prestressing force causes axial deformation of the column. In turn, the axial deformation of the column will cause shortening of the prestressed tendons. λ is used to revise the axial deformation of the column and is defined by Eq. (37).

$$\lambda = \frac{\Delta l'}{\Delta l' + \Delta h} \tag{37}$$

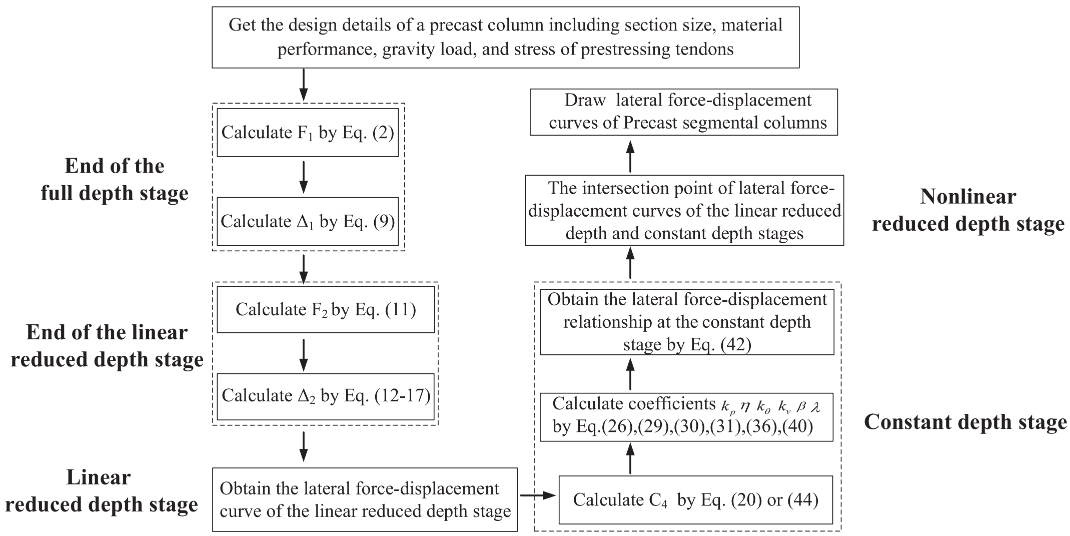

Fig. 7. Calculation flow chart of lateral force–displacement response for precast segmental column.

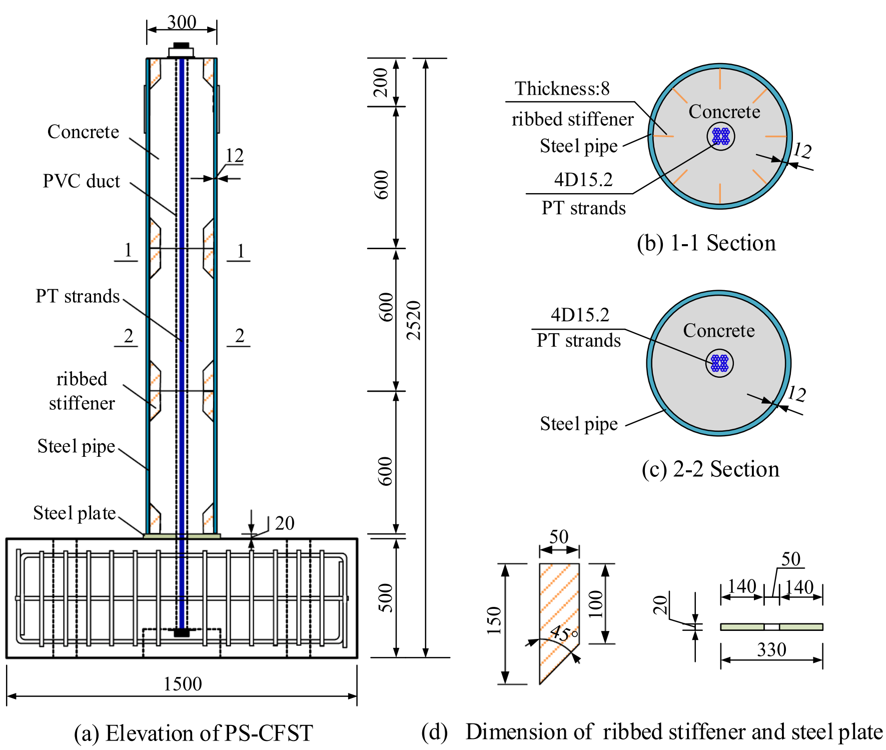

Fig. 8. Configuration and section design of PS-CFST column (Unit: mm).

where Δh is the elongation of the column along with its height. $\Delta l'$ and Δh can be calculated as.

$$\Delta l' = \frac{F_s l}{E_p A_p} \tag{38}$$

$$\Delta h = \frac{F_s h}{EA} \tag{39}$$

Substituting Eqs. (38), (39) into Eq. (37) gives.

$$\lambda = \frac{1}{1 + \frac{A_p E_p h}{AEl}} \tag{40}$$

The elongation of prestressed tendons is closer to the result calculated based on the rigid body assumption. λ is equal to 1 when the column is a rigid body.

To calculate the actual elongation of prestressed tendons, the Δ_4 in Eq. (25) is multiplied by η, β, and λ. Then, Eq. (25) is modified to Eq. (41), considering the effects of bending and shear deformations of the column, the deformation of the bottom interface, and the vertical deformation of the column.

$$\Delta F_{si} = k_p \eta \beta \lambda \Delta_4 \tag{41}$$

Substituting Eqs. (29), (36), (41) into Eq. (19), it gives.

$$F_4 = \frac{(P + F_{si})\frac{D-2d}{2} + \left(\frac{k_p \lambda (D-2C_4)(D-2d)}{2D} - P\right)\Delta_4}{h + \frac{k_p \lambda (K_\theta + K_v)(D-2C_4)(D-2d)}{2DK_\theta K_v}} \tag{42}$$

Table 1
Properties of the materials.

Material	Elastic Modulus E (GPa)	Poisson's ratio υ	Yield Strength (MPa)	Ultimate strength (MPa)	Compressive strength f_c (MPa)	Tensile strength f_t (MPa)
Steel tube	200	0.3	320	420	—	—
Strand	190	0.3	1690	1860	—	—
Concrete	32.9	0.2	—	—	32.9	2.64

Finally, the lateral force–displacement relationship at the nonlinear reduced depth stage is obtained by extending the lines of the linear reduced depth and constant depth stages. The calculation flow chart of lateral force–displacement response for precast segmental columns is shown in Fig. 7.

4. Quasi-static test of PS-CFST bridge column

In order to verify the accuracy of the proposed simplified analytical model, a PS-CFST column was designed, then tested under lateral cyclic loading. As shown in Fig. 8, the PS-CFST column contains three assembled concrete-filled steel tubular segments and a footing with the dimensions of 300 × 300 × 600 mm (length × width × height) and 1000 × 1000 × 500 mm, respectively. The thickness of the steel tube was 12 mm. The loading point of the PS-CSFT was 1800 mm from the top of the footing. To avoid serious damage to segments during loading, ribbed stiffeners with a thickness of 8 mm were welded to both ends of each steel pipe. Furthermore, a 20 mm thick steel plate was installed between the footing and the bottom segment to prevent the concrete crushing of the footing. Four D15.2 prestressed tendons were located in the center of the section to avoid yielding when the column was subjected to maximum drift[39]. The tendons were anchored at the bottom of the footing and passed through three segments. Before the test, the tendons were post-tensioned by an oil jack to an initial prestressing force F_{si}. The gravity load P was applied to simulate the weight of the bridge superstructure. The total axial compression ratio N of the PS-CFST column was defined as the sum of the axial compression ratio N_P and N_F respectively led by gravity load P and initial prestressing force F_{si}, is computed by Eq.(43). According to Specification for Seismic Design of Highway Bridges (JTG/T B02-01–2008) in China[54], the total axial compression ratio N of the bridge column should be less than 0.3 for regular bridge structures. For the PSBC, Hewes[5] suggested that the total axial compression ratio N should be less than 0.2 to ensure excellent ductility. In the study of Dawood et al, an initial prestress in the range of 40 %-60 % of tendon yield strength was recommended to ensure the elasticity of prestressed tendons under maximum lateral displacement. Based on the specification and suggestions, the gravity load P and initial prestressing force F_{si} were set as 500 kN and 400 kN, and the corresponding N_P and N_F were 0.09 and 0.07, respectively. Therefore, the total axial compression ratio N was 0.16.

$$N = N_p + N_F = \frac{P + F_{si}}{f_c A_c + f_y A_s} \tag{43}$$

In which, f_c is the compressive strength of concrete, f_y is the yield strength of steel tube, A_c and A_s are the cross-sectional area of the concrete and steel tube.

The material properties used in the test were obtained based on specific standards and procedures. The results are listed in Table 1. According to the regulation from GB/T228.1–2010[49], tensile tests of steel pipes and prestressed tendons were conducted. The average yield and ultimate strength of the steel pipes were 320 MPa and 420 MPa. The average yield and ultimate strength of the prestressed tendons were 1690 MPa and 1860 MPa. The concrete strength of the PS-CFST column on the day of the experiment was tested based on the standard GB/T50081-2010[48], the tensile strength of concrete was 2.64 MPa, and the averaged 150 × 150 × 150 mm cubic compressive strength $f_{cu,k}$ was 41.6 MPa, corresponding compressive strength f_c was 0.79 $f_{cu,k}$, 32.9 MPa[50].

The PS-CFST column was tested under a constant axial compression loading and a lateral cyclic quasi-static loading. The test setup of the PS-CFST column is shown in Fig. 9. As shown in Fig. 9(a), the footing was fixed to a rigid ground floor by four PT rods. A vertical hydraulic jack was connected to the top of the column to apply the vertical gravity load of 500 kN. A horizontal actuator was connected to a reaction wall at one end and to the top of the column at the other to apply the lateral cyclic load. The lateral load was applied in a displacement control mode. The

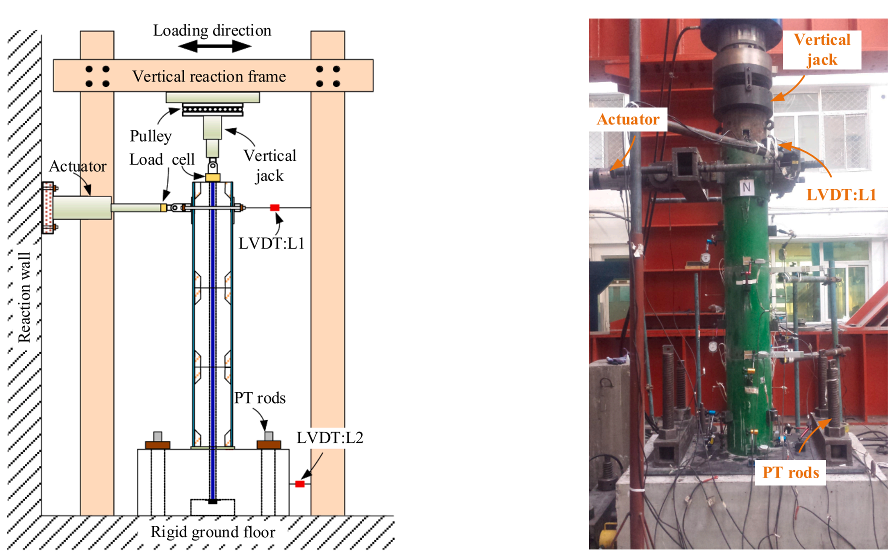

（a）test setup and instrumentations （b）picture of PS-CFST under test

Fig. 9. Testing schematic diagram and picture of PS-CFST column.

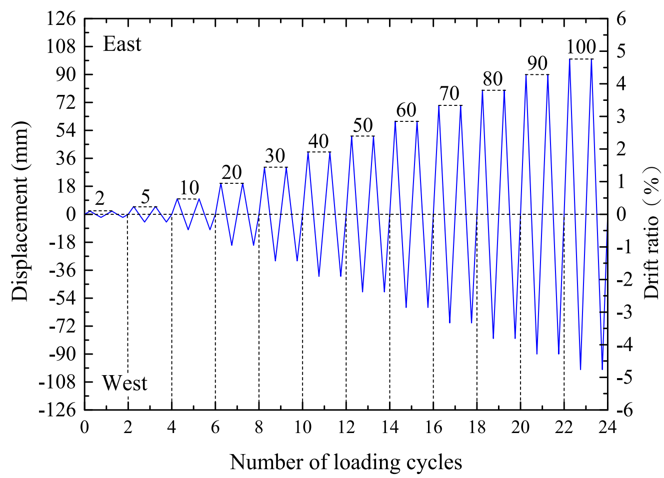

Fig. 10. Loading protocol.

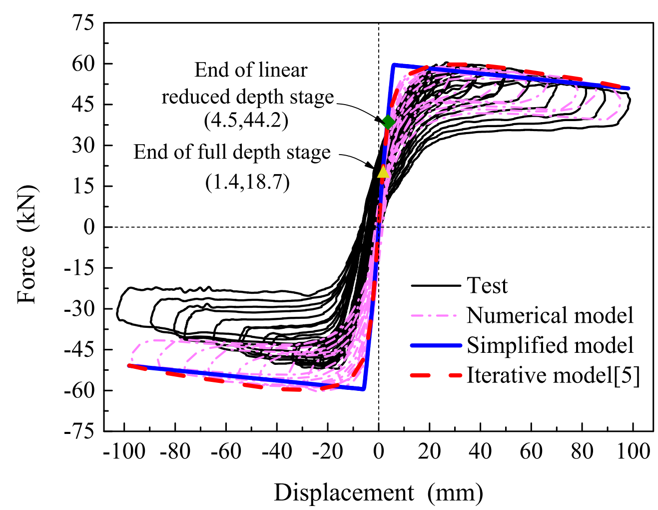

Fig. 11. Comparison of test, numerical, simplified and iterative models results for PS-CFST column.

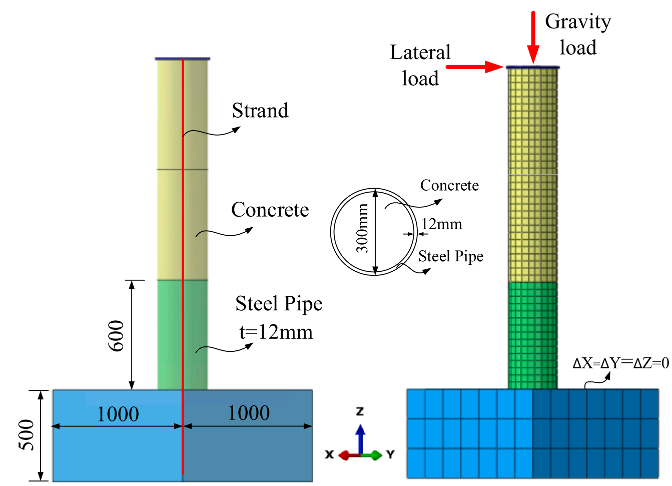

Fig. 12. 3D finite model for the circular concrete-filled steel tube prefabricated column (Unit: mm).

loading protocol is shown in Fig. 10, twelve loading levels are used for the PS-CFST column, the first three lateral loading levels are 2 mm,5 mm and 10 mm, then the subsequent loading level is 10 mm larger than the previous level. The test setup of the PS-CFST column is shown in Fig. 9 (b). The test was stopped when the lateral force dropped to 85 % of the peak load of the PS-CFST column.

Linear differential transducers (LVDT) and loading cells were installed at specific locations to monitor respectively the lateral displacements and forces of the PS-CFST column. As shown in Fig. 9(a), one LVDT, L1 is installed horizontally on the top of the column to monitor applied cyclic displacement Δ, the other LVDT, L2 is mounted at the center height of the footing to measure the slippage of the footing. The lateral force F is recorded by a loading cell placed between the horizontal actuator and the column top. The vertical gravity load is monitored by a loading cell installed between the vertical jack and the column top. The hysteretic loops of the PS-CFST column are obtained by plotting the lateral force F against the lateral displacement Δ. As shown in Fig. 11, the hysteretic curve of the PS-CFST column is in flag-shaped behavior, which results in a small residual displacement and excellent re-centering capacity. However, hysteretic loops are asymmetrical during the loading and unloading stages. The reason is that the uneven contact surface between segments led to irreversible slippage between the bottom segment and the steel plate. In addition to verify the proposed simplified analytical model, the hysteretic curve would also be used to verify the numerical simulation model below.

5. Nonlinear regression analysis of neutral axis depth C_4

In this section, a 3D solid finite element model was firstly established according to the design details of the PS-CFST column and verified by the test result. Then, based on the verified model, 48 cases were compiled to set up an equation predicting the constant neutral axis depth C_4 of PS-CFST columns at constant depth stage. The 3D finite model of the PS-CFST column is shown in Fig. 12. As seen in the figure, the concrete of the segments and footing was simulated by a three-dimensional 8-node solid reduction integration (C3D8R) element. The steel tube was modeled by a 4-node doubly curved shell reduction integration (S4R) element. The tendon was modeled using a 2-node linear 3-D truss (T3D2) element. Only the tensile behavior of the prestressed tendon was considered, while its bending resistance was not. The mesh sizes of the footing, concrete segments and steel tube were 150 mm, 39 mm and 39 mm, respectively.

As shown in Fig. 13, the compression and tension behavior of concrete were modeled by the concrete damaged plasticity (CDP) model based on China Code GB 50010–2010[50]. The peak compressive strength f_c was 32.9 MPa, and the corresponding strain was 0.0012. The peak tensile strength f_t was 2.64 Mpa. The elastic modulus E for compression and tension was 32.9 GPa. The d_c and d_t in Fig. 9 are the damage factors of compression and tension respectively. The values can be calculated based on the China Code GB 50010–2010 in China[50]. In addition, five plasticity parameters must be defined to develop the plastic behavior of concrete in ABAQUS, and the values are shown in Table 2. Because the tendons did not yield during lateral loading, the elastic stress–strain model was used for the prestressed tendons. The elastoplastic stress–strain relationship was adopted for the steel tube.

The contact behavior between steel tube and concrete was modeled by surface-to-surface element. The normal behavior was driven by hard contact, while tangential behavior was defined by tangential friction with a penalty function. The friction coefficient between steel and concrete was between 0.3 and 0.7 in Literature [51], and between 0.57 and 0.7 in Literature [52]. Thus 0.6 was selected as a typical value for the coefficient of friction of the steel-on-concrete contact. Similarly, the surface-to-surface element was adopted to model concrete-on-concrete contact, and different friction coefficient values between segments were used by the previous studies[1333–34], such as 0.3, 0.4, 0.5, etc. The friction coefficient was 0.5 due to the presence of stiffeners in this paper. Two small ends of the prestressed tendons were embedded in the upper end and base of the PS-CFST column to simulate anchorages, no

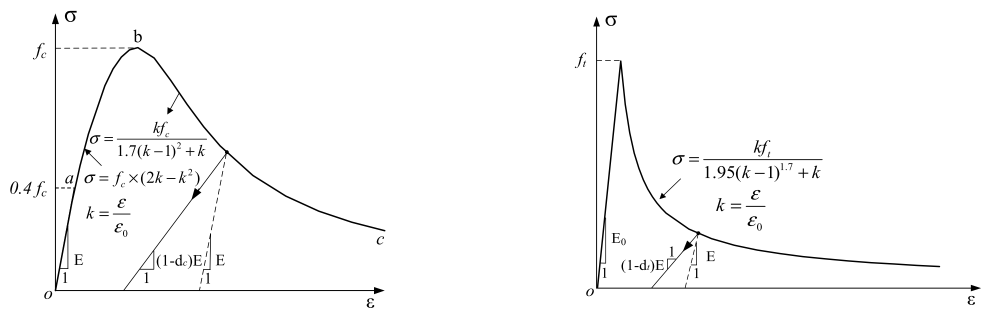

(a) Compressive constitutive model (b) Tensile constitutive model.

Fig. 13. Stress–strain constitutive models of concrete material.

Table 2
Plastic damage parameters of concrete.

Expansion angle	Flow offset	σ_{bo}/σ_{co}	K_c	Viscosity coefficient
30°	0.1	1.16	0.667	0.0005

Note: σ_{bo} is the initial equibiaxial compressive yield stress; σ_{co} is the initial uniaxial compressive yield stress; K_c is the coefficient to define the shape of the deviatoric cross-section.

Table 3
Comparison of analytical, numerical and experimental results.

Method	Δ_1(mm)	F_1 (kN)	Δ_2(mm)	F_2 (kN)
Test result	1.45	17.26	5.1	44.03
Analytical model	1.38	18.75	4.53	44.18
FEA model	1.27	17.7	4.5	44.2
Deviation between test and FEA	12.4 %	2.5 %	11.7 %	0.4 %
Deviation between test and analytical model	4.8 %	8.6 %	13.3 %	0.34 %

contact was set between the middle part and the PS-CFST column.

There were three steps in the finite element model. At the initial step, interactions, boundary conditions and prestressing force were created. For the boundary conditions, the bottom of the column was fixed during the whole analysis. The prestressing force was applied by the initial stress. The axial load was applied to the top of the column using a concentrated force in the second step. In the last step, lateral cyclic load, which was consistent with the quasi-static test, was imposed on the side of the column top. The P-Δ effect was considered throughout the whole analysis.

The force–displacement curves obtained from the test and numerical model are shown in Fig. 11. Table 3 shows the displacements and forces at the key points for the test and numerical model. The deviations between the test and numerical model were less than 12.4 %. The modeling technique and input parameters of the numerical model were verified by the test result.

Based on the validated numerical model, a database including 48 cases was compiled to set up an equation predicting the neutral axis depth C_4 of the PS-CFST column at the constant depth stage. As shown in Table 4, the database contained three independent variables, respectively were the diameter-steel thickness ratio T, the total axial ratio N and the yield strength of steel tube Q. Factorial design was employed,

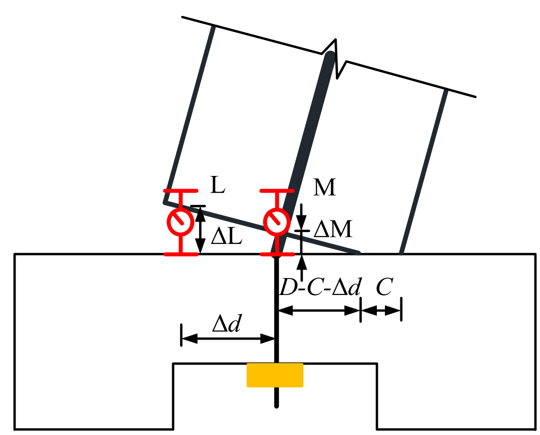

Fig. 14. Calculation of the neutral axis depth.

Table 4
Parametric analysis cases.

Case	Case name	D (mm)	T	P (kN)	F_{si} (kN)	N	Q (MPa)
1	T50N0.16Q235	300	50	500	400	0.16	235
2	T50N0.16Q290	300	50	500	400	0.16	290
3	T50N0.16Q345	300	50	500	400	0.16	345
4	T50N0.16Q390	300	50	500	400	0.16	390
5–8	T33N0.16Q235-T33N0.16Q390	300	33.3	500	400	0.16	235–390
9–12	T25N0.16Q235-T25N0.16Q390	300	25	500	400	0.16	235–390
13–16	T50N0.16Q235-T50N0.16Q390	300	50	400	300	0.132	235–390
17–20	T33N0.132Q235-T33N0.132Q390	300	33.3	400	300	0.132	235–390
21–24	T25N0.132Q235-T25N0.132Q390	300	25	400	300	0.132	235–390
25–28	T50N0.1Q235-T50N0.1Q390	300	50	330	200	0.1	235–390
29–32	T33N0.1Q235-T33N0.1Q390	300	33.3	330	200	0.1	235–390
33–36	T25N0.1Q235-T25N0.1Q390	300	25	330	200	0.1	235–390
37–40	T50N0.068Q235-T50N0.068Q390	300	50	200	200	0.068	235–390
41–44	T33N0.068Q235-T33N0.068Q390	300	33.3	200	200	0.068	235–390
45–48	T25N0.068Q235-T25N0.068Q390	300	25	200	200	0.068	235–390

Note: T50N0.16Q235 means that the diameter-steel thickness ratio is 50, the total axial ratio is 0.16, the yield strength of steel is 235 MPa.

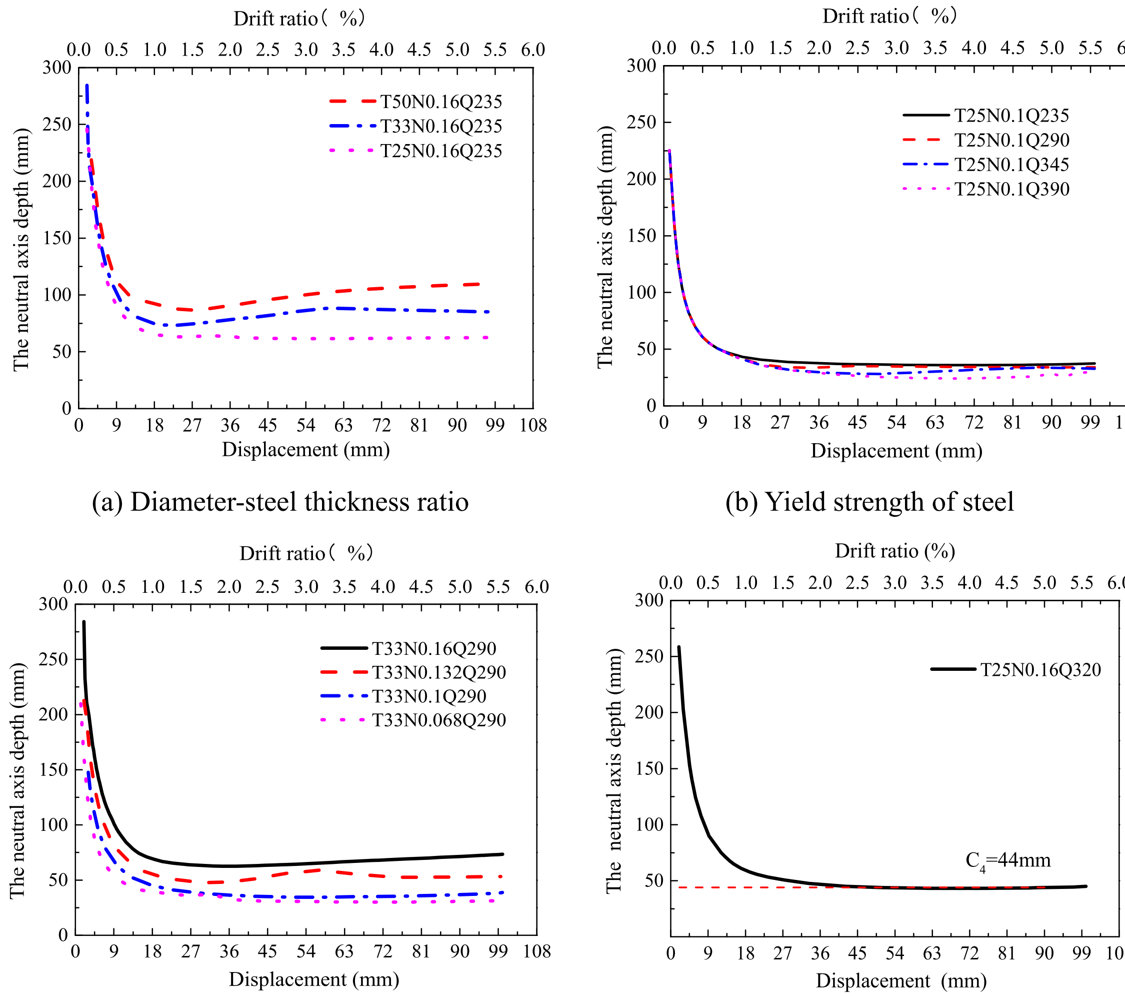

(a) Diameter-steel thickness ratio
(b) Yield strength of steel
(c) Total axial compression ratio
(d) Neutral axis depth of PS-CFST column

Fig. 15. Effect of different parameters on the neutral axis depth of PS-CFST column.

the diameter-steel thickness ratio T comprised 50, 33.3, 25, the total axial ration N comprised 0.16, 0.132, 0.1, 0.68, the yield strength of steel Q comprised 235 MPa, 290 MPa, 345 MPa, 390 MPa. It should be noted that pushover analysis was used to obtain the neutral axis depths of 48 cases for high computational efficiency.

The neutral axis depths of the 48 models were calculated by Eq. (43). As shown in Fig. 14, the vertical displacements of points L and M (ΔL, ΔM), and the horizontal distance (Δd) between them were obtained from models to calculate the neutral axis depths. The neutral axis depth-lateral displacement curves of some cases are illustrated in Fig. 15. Minor changes in the neutral axis depth could be observed when the drift ratio was larger than 1.5 %. Thus, C_4 was considered a constant as described above. As shown in Fig. 15d, here, the C_4 is 44 mm for the simulated PS-CFST column.

$$C_4 = D - \Delta d - \frac{\Delta M \Delta d}{\Delta L - \Delta M} \tag{43}$$

Based on the neutral axis depths of 48 cases calculated by Eq.(43), Eq.(44) was obtained by nonlinear regression analysis.

$$C_4/D = 0.09T^{0.78334}N^{0.939}(Q/235)^{-0.90534} \tag{44}$$

The R2 of Eq. (44) was 95%, it indicated that the equation had a 95% fit. Fig. 16 also shows the high accuracy of the predicted equation. The NAD $C4$ increases with the increasing T and N, whereas decreases with the increasing Q. The predicted $C4$ by Eq. (44) is 45.4 mm for the

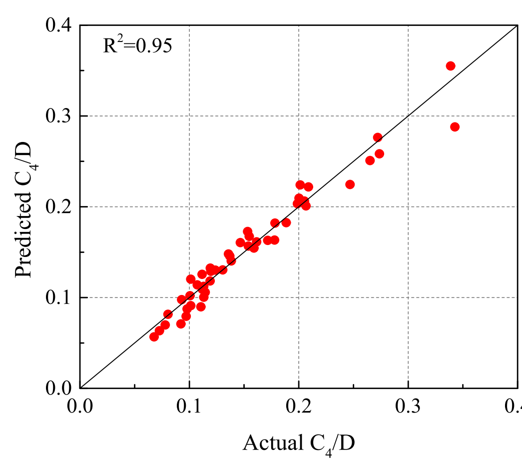

Fig. 16. Differences between the predicted and actual C4/D.

simulated PS-CFST column in this research, the deviation is 3% between the predicted and actual value (44 mm). There are two reasons that account for the deviation. One is that a small change of the NAD at the constant depth stage exists, but it is regarded as a constant in the study. The other is that the boundary line between compression and tension is

Table 5
Comparison of test, simplified and iterative models.

Method	Peak strength (kN)			Lateral stiffness (kN/mm)		
	PS-CFST	JH1 [5]	Specimen 1 [53]	PS-CFST	JH1 [5]	Specimen 1 [53]
Test result	60.4	216.6	200	12.0	13.1	12.1
Simplified model	59.6	217.7	197	13.3	12.5	14.0
Iterative model	59.8	220.7	196.8	13.1	11.9	14.1
Test result/ Simplified model	1.01	0.99	1.02	0.90	1.05	0.86
Test result/ Iterative model	1.01	0.98	1.02	0.92	1.10	0.86

not straight.

6. Verification of the simplified analytical model

The monotonical force–displacement curve of the PS-CFST column, namely the backbone curve, can be obtained by connecting the peak value of each cycling loop. The simplified analytical model of the backbone curve for the PS-CFST column was calculated according to the proposed method. The result is shown in Fig. 11, the lateral force capacity of the PS-CFST column obtained from the proposed simplified analytical model has a favorable agreement with the experimental and numerical results. The experimental, analytical and numerical displacements and forces at the ends of the full depth and linear reduced depth stages are summarized in Table 3, and the max deviation between the analytical model and test is 13.3 %. In addition, the lateral force–displacement curve of the PS-CFST column was calculated based on the iterative model proposed by Hewes[5]. The result is also shown in Fig. 11, the shape of the lateral force–displacement curves of simplified and iterative models are approximately the same. The peak lateral capacity and lateral stiffness of the PS-CFST obtained by test, simplified and iterative models are listed in Table 5. It is found that the peak strength ratio of the simplified model to either the test or iterative model is close to 1. The same result is found in the lateral stiffness ratio. It is indicated that the simplification of the lateral force–displacement curve at the nonlinear reduced depth stage has minor effect on predicting the peak lateral capacity and lateral stiffness of the PS-CFST column.

To prove the generalization of the simplified model, two typical published experimental studies on the seismic performance of the precast segmental columns were selected. One is an SC-PSBC, denoted as “JH1” in the study of Hewes[5], the other is a precast segmental concrete-filled steel tube column, named “Specimen 1” in the study of Chou and Cheng[53]. The lateral force–displacement curves of the test, simplified and iterative models of “JH1” and “specimen 1” are shown separately in Fig. 17(a) and Fig. 17(b). As seen in the figure, the lateral force–displacement curves of the test, simplified and iterative models are in good agreement. The peak lateral strength and lateral stiffness of “JH1” and “specimen 1” are listed in Table 5, their ratios of the test and simplified model, or iterative model are close to 1. The computation procedure of lateral force–displacement response for “JH1” is shown in Appendix.

7. Parameter analysis of the simplified analytical model for PS-CFST

According to Eqs. (26), (40) and (42), when the geometry and material properties of the PS-CFST column are specified, the lateral force capacity of the column is affected by the initial prestressing force, area of the prestressed tendons and gravity load. The influences of these three factors on the lateral force capacity of the PS-CFST column were investigated by the proposed analytical model. 7 cases with different PS-CFST column parameters are listed in Table 6.

Cases 1, 2 and 3 were to investigate the influence of the initial prestressing force, the initial tendon stresses of 20 %, 30 %, 38 % of ultimate strength for each prestressed tendon were used. Case 1 was the reference column, which was the same as the PS-CFST column subjected to the quasi-cyclic loading. The force–displacement curves of the PS-CFST column are illustrated in Fig. 18a. The post-yield stiffness varies from −0.057 to −0.082. The differences in the post-yield stiffness among the PS-CFST columns with various initial prestressing forces are not significant. The displacements and corresponding forces at the ends of the full depth and linear reduced depth stages are summarized in Table 7. The results indicate that the displacements and corresponding forces at the ends of full depth and linear reduced depth stages increase with the

Table 6
Specimens with different design parameters.

No	Case Name	F_{si} (kN)	A_p (mm^2)	P (kN)
1	F_{si}-38 % /A_p-0.8 %/P-0.09	400	560 (4D15.2)	500
2	F_{si}-20 %	208	560 (4D15.2)	500
3	F_{si}-30 %	312	560 (4D15.2)	500
4	A_p-0.6 %	400	420 (3D15.2)	500
5	A_p-1 %	400	700 (5D15.2)	500
6	P-0.054	400	560 (4D15.2)	300kN
7	P-0.07	400	560 (4D15.2)	400

Note: The number in front of D15.2 represents the number of prestressed tendons with a diameter of 15.2.

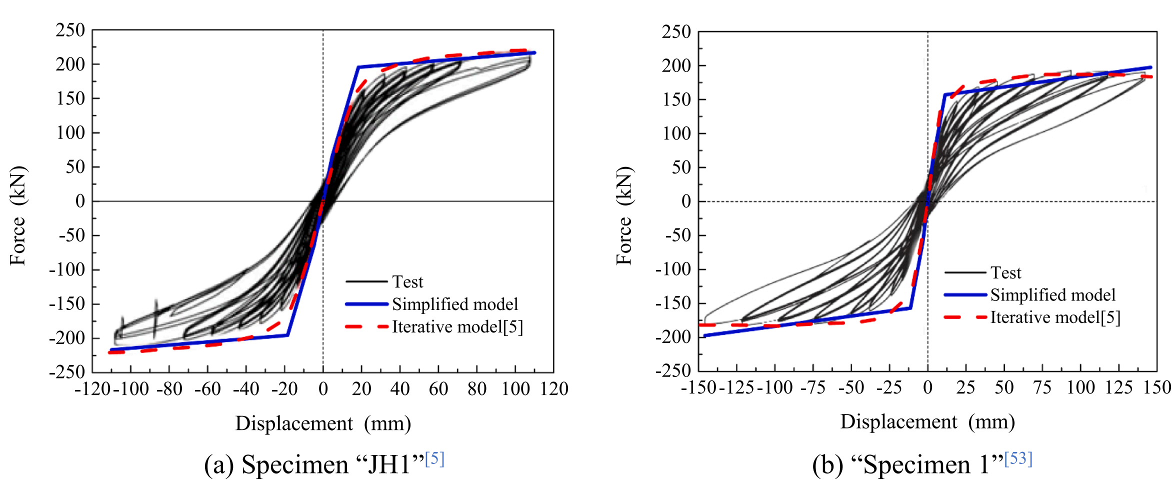

Fig. 17. Comparison of the lateral force–displacement curves of test, simplified and iterative models.

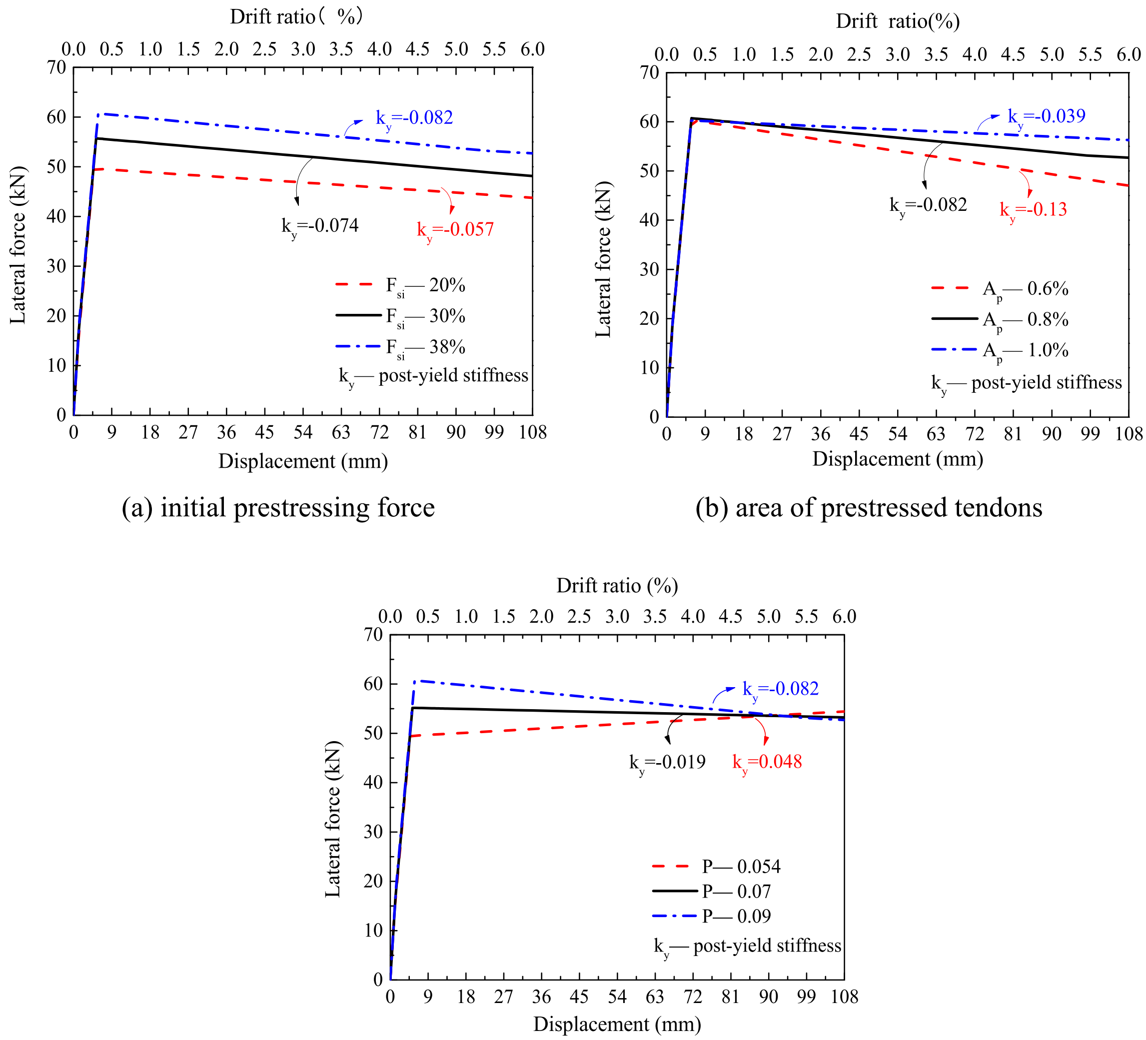

(a) initial prestressing force

(b) area of prestressed tendons

(c) gravity load

Fig. 18. Influence of various parameters on the lateral force capacity of PS-CFST.

Table 7
Displacements and forces of the PS-CFST columns at the full depth and linear reduced depth stages.

No	Case name	Δ_1(mm)	F_1 (kN)	Δ_2(mm)	F_2 (kN)
1	F_{si}-38 %/A_p-0.8 %/P-0.09	1.38	18.75	4.04	44.18
2	F_{si}-20 %	1.08	14.5	3.18	34.75
3	F_{si}-30 %	1.24	16.9	3.65	39.86
4	A_p-0.6 %	1.38	18.75	4.04	44.18
5	A_p-1 %	1.38	18.75	4.04	44.18
6	P-0.054	1.07	14.58	3.15	34.36
7	P-0.07	1.22	16.67	3.6	39.27

increasing initial prestressing force, which also causes an increase in the peak strength of the PS-CFST column. The same result can be found in the literatures [39–40].

The effect of the prestressed tendons area was investigated by cases 1,4 and 5, the reinforcement ratios of prestressed tendons respectively were 0.6 %, 0.8 %, 1 %. The results are shown in Fig. 18b. It can be seen that the reinforcement ratio of the prestressed tendon has a significant effect on the post-yield stiffness of the PS-CFST column. The PS-CFST column with the higher reinforcement ratio of prestressed tendons has a higher post-yield stiffness. However, as shown in Table 7, the displacements and corresponding forces at the ends of the full depth and linear reduced depth stages are the same in cases 1, 4 and 5. It implies that the reinforcement ratio of prestressed tendons does not influence the response of the PS-CFST column at the full depth and linear reduced depth stages.

Cases 1, 6 and 7 were used to evaluate the influence of the gravity load on the response of the PS-CFST column, the axial load ratios of 0.054, 0.07, 0.09 resulting from gravity were considered. As shown in Fig. 18c, the axial load ratio affects both the post-yield stiffness and lateral strength of the PS-CFST column, which is different from the initial prestressing force and area of the prestressed tendons. With increasing gravity, the lateral capacity of the PS-CFST column increases, whereas the post-yield stiffness decreases. In addition, the post-yield stiffness of the PS-CFST column is negative when the axial ratio resulting from gravity is more than 0.054. It implies that a high axial ratio of the PS-CFST column leads to a drop in the lateral strength and ductility of the PS-CFST column.

8. Conclusions

In order to simplify the calculation of the lateral force capacity of unbonded post-tensioned precast segmental columns, a simplified analytical model without iteration was proposed considering the neutral axial depth, which tends to be a constant value during the loading process. A regression equation to predict the constant value was developed by 48 numerical simulation cases. The proposed simplified analytical model was verified by the results from the experimental test and verified finite element model. The following conclusions can be derived.

(1) The proposed simplified analytical model can predict the lateral force–displacement behavior of precast bridge columns accurately without iterative calculations. The calculation process is simple and efficient, predicted results meet the engineering calculation accuracy requirements, and it is more suitable for application in engineering design.
(2) The predicted equation of the constant value of neutral axis depth of PS-CFST columns was developed by nonlinear regression analysis, which passed the F test (P value less than 0.05), and had a higher R^2 (95 %). The constant value is positively related to axial ratio and diameter-thickness ratio, and negatively related to yield strength of steel tube of PS-CFST column.
(3) The lateral force capacity of the SC-PSBC and PS-CFST column obtained from the proposed simplified analytical model has a favorable agreement with the test result.
(4) When the geometry and material properties of PS-CFST columns are specified, the column with the lower gravity load and the higher reinforcement ratio of prestressed tendons would achieve the larger post-yield stiffness. The increase of the gravity load and initial prestressing force would improve the lateral strength of PS-CFST columns.

Uncited references

CRediT authorship contribution statement

Kaidi Zhang: Writing – original draft, Writing – review & editing, Software, Formal analysis, Data curation. **Junfeng Jia:** Writing – original draft, Methodology, Investigation, Visualization, Data curation, Funding acquisition. **Ning Li:** Writing – review & editing, Investigation, Validation. **Jianyu Zhao:** . **Yulei Bai:** Investigation, Writing – review & editing.

Declaration of Competing Interest

The authors declare that they have no known competing financial interests or personal relationships that could have appeared to influence the work reported in this paper.

Data availability

Data will be made available on request.

Acknowledgements

This work was financially supported by the International Science & Technology Cooperation Program of China under Grand No. 2019YFE0119800, National Natural Science Foundation of China under Grant No. 52178449, Beijing Natural Science Foundation under Grand No. 8202002. Key Laboratory of Transport Industry of Bridge Detection Reinforcement Technology (Beijing) under Grand No. 2021-JQKFKT-4. Their support is gratefully acknowledged.

Appendix

The design detail of column JH1 could be found in the study of Hewes (Hewes 2002). D = 610 mm, A = 292246.657 mm^2, h = 3660 mm, l = 3356 mm, P = 890 kN, F_{si} = 2230 kN, E = 33 GPa, E_p = 196 GPa, μ_c=0.2, N = 0.22, L_p = 305 mm.

1 F_1 was calculated by Eq. (2):

$$F_1 = \frac{(F_{si}+P)I_g}{0.5DAh} = \frac{(2230+890)\times(\pi\times 610^4/64)}{0.5\times 610\times 292246.66\times 3660} = 65 \quad kN$$

$\Delta_1$2. was calculated by Eq. (9):

$$\Delta_1 = \frac{F_1h^3}{3EI_g} = \frac{65\times 3660^3}{3\times 33\times(\pi\times 610^4/64)} = 4.74 \quad mm$$

3. The distance from the centroid of the compression zone to the center of the bottom interface y:$y = \frac{2D}{3\pi} = \frac{2\times 610}{3\pi} = 129.45\,mm$

4. Moment of inertia at the end of the linear reduced depth stage:$I_{g/2} = \frac{\pi D^4}{128} - \frac{Ay^2}{2} = \frac{\pi\times 610^4}{128} - \frac{292246.66\times 129.45^2}{2} = 949798391.1\,mm^4$

5. F_2 was calculated by Eq. (11):

$$F_2 = \frac{2(F_{si}+P)I_{g/2}}{Ayh} + \frac{y(F_{si}+P)}{h}$$
$$= \frac{2\times(2230+890)\times 949798391.1}{292246.66\times 129.45\times 3660} + \frac{129.45\times(2230+890)}{3660}$$
$$= 153.15 \quad kN$$

6. Δ_2 was calculated by Eq. (17):

$$\Delta_2 = \frac{2F_2h^3 - 3DF_2h^2}{6EI_g} + \frac{DF_2h^2 - yDh(F_{si}+P)}{2EI_{g/2}}$$
$$= \frac{2\times 153.15\times 3660^3 - 3\times 610\times 153.15\times 3660^2}{6\times 33\times 6796561308} + \frac{610\times 153.15\times 3660^2 - 129.45\times 610\times 3660\times(2230+890)}{2\times 33\times 949798391.1}$$
$$= 13.95 \quad mm$$

7. The lateral force$F_{1\text{-}2}$ -displacement Δ_{1-2} response at the linear reduced depth stage could be calaculated:

$$F_{1-2} = \frac{F_2-F_1}{\Delta_2-\Delta_1}\Delta_{1-2} + (F_2 - \frac{F_2-F_1}{\Delta_2-\Delta_1}\Delta_2)$$
$$= 9.57\Delta_{1-2} + 19.7$$

8. C_4, k_p,K_θ, K_V and λ were calculated by Eqs. (20), (26), (30), (31)and(40):

$$C_4 = \frac{1.3\sqrt{N}}{\sqrt{7.7}}D = \frac{1.3\times\sqrt{0.22}}{\sqrt{7.7}}\times 610 = 133.8 \quad mm$$

$$k_p = \frac{0.5DE_pA_p}{hl} = \frac{0.5\times 610\times 196\times 2665}{3660\times 3356} = 12.97 \quad kN/mm$$

$$K_\theta = \frac{2.1EI_g}{h^3} = \frac{2.1\times 33\times 67965561308}{3660^3} = 9.61 \quad kN/mm$$

$$K_V = \frac{E_cA_c}{2(1+\mu_c)h} = \frac{33\times 292246.657}{2\times(1+0.2)\times 3660} = 1097.92 \quad kN/mm$$

$$\lambda = \frac{1}{1+\frac{A_pE_ph}{AEl}} = \frac{1}{1+\frac{2665\times 196\times 3660}{292246.657\times 33\times 3356}} = 0.94$$

9 The lateral force–displacement response at the constant depth stage was calculated by Eq. (42):

$$F_4 = \frac{(P+F_{si})\frac{D-2d}{2} + \left(\frac{k_p\lambda(D-2C_4)(D-2d)}{2D} - P\right)\Delta_4}{h + \frac{k_p\lambda(K_\theta+K_v)(D-2C_4)(D-2d)}{2DK_\theta K_v}}$$

$$= \frac{(890+2230)\times\frac{610-2\times 77}{2} + (\frac{12.97\times 0.94\times(610-2\times 133.8)\times(610-2\times 77)}{2\times 610} - 890)\Delta_4}{3660 + \frac{12.97\times 0.94\times(9.61+1097.92)\times(610-2\times 133.8)\times(610-2\times 77)}{2\times 610\times 9.61\times 1097.92}}$$
$$= 0.23\Delta_4 + 19.7$$

10. The lateral force–displacement relationship of the nonlinear reduced depth stage was obtained by extending the lateral force–displacement curves of the linear reduced depth and constant depth stages, and the intersection point of lateral force–displacement curves of the linear reduced depth and constant depth stages was (18.4 mm,198.5 kN). The lateral force–displacement curves of all stages were drawn, the result of the test and simplified analytical model was shown in Fig. 17, and good agreement between the test and simplified analytical model was found.

References

[1] Ou YC, Tsai MS, Chang KC, Lee GC. Cyclic behavior of precast segmental concrete bridge columns with high performance or conventional steel reinforcing bars as energy dissipation bars. Earthq EngingStruct Dyn 2010;39(11):1181–98. https://doi.org/10.1002/eqe.986.

[2] Routledge P, Mchaffie B, Cowan M, Palermo A. Wigram-Magdala link bridge: low-damage details for a more efficient seismic design philosophy. Struct Eng Int 2020;30(2):177–84. https://doi.org/10.1080/10168664.2019.1679696.

[3] Han Q, Jia ZL, Xu K, Zhou YL, Du XL. Hysteretic behavior investigation of self-centering double-column rocking piers for seismic resilience. Eng Struct 2020;188:218–32. https://doi.org/10.1016/j.engstruct.2019.03.024.

[4] Mander, JB, Cheng CT. Seismic resistance of bridge piers based on damage avoidance design. Report no. NCEER-97-0014. Buffalo (NY): State Univ. of New York; 1997.

[5] Hewes JT. Seismic design and performance of precast concrete segmental bridge columns. Report No. SSRP-2001/25. San Diego: CA: University of California; 2002.

[6] Chou CC, Chang HJ, Hewes JT. Two-plastic-hinge and two dimensional finite element models for post-tensioned precast concrete segmental bridge columns. Eng Struct 2013;46:205–17. https://doi.org/10.1016/j.engstruct.2012.07.009.

[7] Jia JF, Zhao JY, Zhang Q, Qi LK, Han Q, Du XL. Experiment on lateral bearing behavior of post-tensioned segmental CFST bridge pier columns. China J Highw Transp 2017;30:236-245 [in Chinese]. https://doi.org/ 10.19721/j.cnki.10017372.2017.03.026.

[8] Zhang D, Li N, Li ZX. Seismic performance of precast segmental concrete-filled steel-tube bridge columns with internal and external energy dissipaters. J Bridge Eng 2021;26(11):04021085. https://doi.org/10.1061/(ASCE)BE.1943-5592.0001792.

[9] ElGawady MA, Dawood HM. Analysis of segmental piers consisted of concrete filled FRP tubes. Eng Struct 2012;8:142–52. https://doi.org/10.1016/j.engstruct.2012.01.001.

[10] Wang Z, Wang JQ, Tang YC, Liu TX, Gao YF, Zhang J. Seismic behavior of precast segmental UHPC bridge columns with replaceable external cover plates and internal dissipaters. Eng Struct 2018;177:540–55. https://doi.org/10.1016/j.engstruct.2018.10.012.

[11] Billington SL, Yoon JK. Cyclic response of unbounded posttensioned precast columns with ductile fiber reinforced concrete. J Bridge Eng 2004;9(4):353–63. https://doi.org/10.1061/(ASCE)1084-0702(2004)9:4(353).

[12] Palermo A, Pampanin S, Marriott D. Design, modeling, and experimental response of seismic resistant bridge piers with posttensioned dissipating connections. J Struct Eng 2007;133(11):1648–61. https://doi.org/10.1061/(ASCE)0733-9445(2007)133:11(1648).

[13] Ou YC, Chiewanichakorn M, Areaf AJ, Lee GC. Seismic performance of segmental precast unbounded postensioned concrete bridge columns. J Struct Eng 2007;133(11):1636–47. https://doi.org/10.1061/(ASCE)07339445(2007)133:11(1636).

[14] Jia JF, Zhang KD, Wu SW, Guo Y, Du XL, Wang X. Seismic performance of self-centering precast segmental bridge columns under different lateral loading directions. Eng Struct 2020;221:111037. https://doi.org/10.1016/j.engstruct.2020.111037.

[15] Bu ZY, Ou YC, Song JW, Zhang NS, Lee GC. Cyclic loading test of unbonded and bonded posttensioned precast segmental bridge columns with circular section. J Bridge Eng 2016;21:04015043. https://doi.org/10.1061/(ASCE)BE.1943-5592.0000807.

[16] Moon D, Roh H, Cimellaro G. Seismic performance of segmental rocking columns connected with NiTi Martensitic SMA Bars. Adv Struct Eng 2015;18(4):571–84. https://doi.org/10.1260/1369-4332.18.4.571.

[17] Saiidi MS, O'Brien M, Sadrossadat-Zadeh M. Cyclic response of concrete bridge columns using superelastic nitinol and bendable concrete. ACI Struct J 2009;106(1):69–77.

[18] Tazarv M, Saiidi MS. Low-damage precast columns for accelerated bridge construction in high seismic zones. J Bridge Eng 2016;21(3):04015056. https://doi.org/10.1061/(ASCE)BE.1943-5592.0000806.

[19] Wang JC, Ou YC, Chang KC, Lee GC. Large-scale seismic tests of tall concrete bridge columns with precast segmental construction. Earthq Enging Struct Dyn 2008;37:1449–65. https://doi.org/10.1002/eqe.824.

[21] Guo T, Cao ZL, Xu ZK, Lu S. Cyclic load tests on self-centering concrete pier with external dissipators and enhanced durability. J Struct Eng 2016;142(1):04015088. https://doi.org/10.1061/(ASCE)ST.1943-541X.0001357.

[22] ElGawady MA, Sha'lan A. Seismic behavior of self-centering precast segmental bridge bents. J Bridge Eng 2011;16(3):328-339. https://doi.org/10.1061/(ASCE)BE.1943-5592.0000174.

[23] Marriott D, Pampanin S, Palermo A. Quasi-static and pseudo-dynamic testing of unbonded post-tensioned rocking bridge piers with external replaceable dissipaters. Earthq Engng Struct Dyn 2009;38(3):331–54. https://doi.org/10.1002/eqe.857.

[24] Li C, Bi KM, Hao H, Zhang XH, Tin DV. Cyclic test and numerical study of precast segmental concrete columns with BFRP and TEED. Bull Earthq Eng 2019;17(6):1–20. https://doi.org/10.1007/s10518-019-00597-1.

[25] Tong C, Wu J, Li C. A novel precast concrete beam–column connection with replaceable energy-dissipation connector: experimental investigation and theoretical analysis. Bull Earthq Eng 2021;19:4911–43. https://doi.org/10.1007/s10518-021-01144-7.

[26] Ou YC, Pratiwi AY, Song J. Pseudodynamic Testing and Inelastic Displacement Ratios of Self-Centering Precast Concrete Segmental Bridge Columns. J Struct Eng 2018;144(9):413–23. https://doi.org/10.1061/(ASCE)ST.1943-541X.0002161.

[27] Zhou Y-L, Han Q, Du X-L, Jia Z-L. Shaking table tests of post-tensioned rocking bridge with double-column bents. J Bridge Eng 2019;24(8). https://doi.org/10.1061/(ASCE)BE.1943-5592.0001456.
[28] Mantawy IM, Thonstad T, Sanders DH, Stanton JF, Eberhard MO. Seismic Performance of Precast, Pretensioned, and Cast-in-Place Bridges: Shake Table Test Comparison. J Bridge Eng 2016;21(10). https://doi.org/10.1061/(ASCE)BE.1943-5592.0000934.
[29] Twigden KM, Henry RS. Shake table testing of unbonded post-tensioned concrete walls with and without additional energy dissipation. Soil Dyn Earthq Eng 2019;119:375–89. https://doi.org/10.1016/j.soildyn.2018.05.007.
[30] Reggiani Manzo N, Vassiliou MF, Mouzakis H, Badogiannis E. Shaking table tests of a resilient bridge system with precast reinforced concrete columns equipped with springs. Earthq Eng Struct Dyn 2022;51(1):213–39.
[31] Zhang D, Li N, Li Z-X, Xie L. Seismic performance of bridge with unbonded posttensioned self-centering segmented concrete-filled steel-tube columns: An underwater shaking table test. Soil Dyn Earthq Eng 2020;138:106350.
[32] Hassanli R, Youssf O, Mills JE, Karim R, Vincent T. Performance of Segmental Self-centering Rubberized Concrete Columns under Different Loading Directions. J Build Eng 2018;20:285–302.
[33] Li C, Hao H, Bi KM. Seismic performance of precast concrete-filled circular tube segmental column under biaxial lateral cyclic loadings. Bull Earthq Eng 2019;17(1):271–96. https://doi.org/10.1007/s10518-018-0443-4.
[34] Li C, Bi KM, Hao H. Seismic performances of precast segmental column under bidirectional earthquake motions: Shake table test and numerical evaluation. Eng Struct 2019;187:314–28. https://doi.org/10.1016/j.engstruct.2019.03.001.
[35] Benjumea J, Saiidi MS, Itani A. Large-Scale Biaxial Shake-Table Studies of a Precast Bridge Model. J Struct Eng 2021;147(7):07339445. https://doi.org/10.1061/(ASCE)ST.1943-541X.0003060.
[36] Li C, Hao H, Bi KM. Numerical study on the seismic performance of precast segmental concrete columns under cyclic loading. Eng Struct 2017;148:373–86. https://doi.org/10.1016/j.engstruct.2017.06.062.
[37] Shen Yu, Liu X, Li Y, Li J. Cyclic tests of precast post-tensioned concrete filled steel tubular (PCFT) columns with internal energy-dissipating bars. Eng Struct 2021;229:111651.
[38] Tong T, Zhuo W, Jiang X, Lei H, Liu Z. Research on seismic resilience of prestressed precast segmental bridge piers reinforced with high-strength bars through experimental testing and numerical modelling. Eng Struct 2019;197:109335.
[39] Zhang D, Li N, Zhang S. Energy dissipation and resilience of precast segmented concrete-filled steel tube self-centering column: Parameter study and design methodology. Eng Struct 2021;244:112747. https://doi.org/10.1016/j.engstruct.2021.112747.
[40] Dawood H, Elgawady M, Hewes J. Factors affecting the seismic behavior of segmental precast bridge columns. Front Struct Civ Eng 2014;8(4):388–98.
[41] Wang Z, Wang JQ, Zhao GT, Zhang J. Design criterion for the self-centering capacity of precast segmental UHPC bridge columns with unbonded post-tensioning tendons. Eng Struct 2019;200:109706. https://doi.org/10.1016/j.engstruct.2019.109706.
[42] Bu ZY, Guo J, Zheng RY, Song JW, Lee GC. Cyclic performance and simplified pushover analyses of precast segmental concrete bridge columns with circular section. Earthq Eng Eng Vib 2016;15(2):297–312. https://doi.org/10.1007/s11803-016-0323-3.
[43] Bu ZY, Ou YC. Simplified analytical pushover method for precast segmental concrete Bridge columns. Adv Struct Eng 2013;16(5):805–22. https://doi.org/10.1260/1369-4332.16.5.805.
[44] Bu ZY, Zhang X, Ye HH, Kang X. Multi-joint rotation analytical pushover method for precast segmental bridge columns and experimental validation. China J Highw Transp 2017;30(12):258-267 [in Chinese]. https://doi.org/ 10.19721/j.cnki.1001-7372.2017.12.028.
[46] Wang Z, Wang JQ, Liu TX, Zhang J. An explicit analytical model for seismic performance of an unbonded post-tensioned precast segmental rocking hollow pier. Eng Struct 2018;161:176–91. https://doi.org/10.1016/j.engstruct.2018.02.025.
[47] Beijing : China Architecture & Building Press 2014 [in Chinese].
[48] Beijing: China Communications Press 2008 [in Chinese].
[49] Beijing: China Architecture & Building Press 2010 [in Chinese].
[50] Beijing : China Architecture & Building Press 2010 [in Chinese].
[51] Eligehausen R, Mallee R, Silva JF. Anchorage in concrete construction. Stuttgart, Germany: Ernst & Sohn Press; 2006.
[52] Rabbat BG, Russell HG. Friction coefficient of steel on concrete or grout. J Struct Eng 1985;111(3):505515.https://doi.org/10.1061/(ASCE)07339445(1985)111:3(505).
[53] Chou CC, Chen YC. Cyclic tests of post-tensioned precast CFT segmental bridge columns with unbonded strands. Earthq Eng Struct Dyn 2006;35:159–75. https://doi.org/10.1002/eqe.512.
[54] Ministry of Transport of the People's Republic of China. Guidelines for Seismic Design of Highway Bridges (JTG/T B02-01-2008). Beijing: China Communications Press; 2008 [in Chinese].